Journal of the Serbian Society for Computational Mechanics / Vol. 15 / No. 2, 2021 / pp 10-22
(10.24874/jsscm.2021.15.02.02)

MOLECULAR DYNAMICS OBSERVATION OF DISCRETENESS OF THE MASS DISTRIBUTION DURING NANOSCALE FRAGMENTATION

Sreten Mastilović

Institute for Multidisciplinary Research, University of Belgrade, Belgrade, Serbia
e-mail: misko.mastilovic@imsi.bg.ac.rs

Abstract

Molecular dynamics simulations of the rigid-anvil collision test are performed by using a two-dimensional computational setup that mimics the traditional ballistic Taylor test. In this extensively utilized computational setup, the slender nanoscale projectiles collide with a rigid wall with hypersonic striking velocities ranging from 3 km/s to 30 km/s. The projectiles used in these simulations are flat-ended, monocrystalline, nanoscale bars prepared at zero temperature. The Poisson hyper-exponential distribution with the logarithmic binning is used to capture the fragment mass (size) distribution under the constraint of the relatively small specimen size 15×100 nm. The objective is to highlight the occurrence of certain discreteness of the fragment mass distribution observed both in time (during the fragment debris evolution) and across the striking velocity field (for the final fragmentation states that correspond to the stationary distributions).

Keywords: Taylor test, impact fragmentation, discreteness, fragment mass distribution

1. Introduction

The ballistic Taylor test is a classic method for investigation of dynamic behavior of materials subjected to the extreme levels of plastic distortion (Fig. 1). For the range of striking velocities used in the present study, the extremity of the loading powers involved and the corresponding plastic distortion (schematically represented by Fig. 1b) results in the dynamic fragmentation of the nanoprojectile (Fig. 1c, Fig. 2 and Fig. 3b). A series of two-dimensional (2D) classic MD (molecular dynamics) simulations of the ballistic Taylor test (Fig. 1a) is performed with a main objective to explore a certain aspects of discreteness of the fragment mass distribution observed in these MD simulations. The slender, flat-ended nanoprojectiles utilized in the present investigation are made of a monocrystalline Lennard-Jones solid with an implicit supposition that the simplicity of this generic model does not impede the qualitative investigation of this unique and intriguing feature of the nanoscale fragmentation. The striking velocities (v) vary in a wide hypervelocity range from 3 km/s to 30 km/s. The lower bound of this range corresponds to the onset of the complete fragmentation (just sufficient to fully fragment the projectile without a residual stump, Fig. 2b) as established in a previous study (Mastilović 2015). The upper bound of this range comfortably exceeds the current speed of man-made projectiles but not necessarily those encountered by space structures.

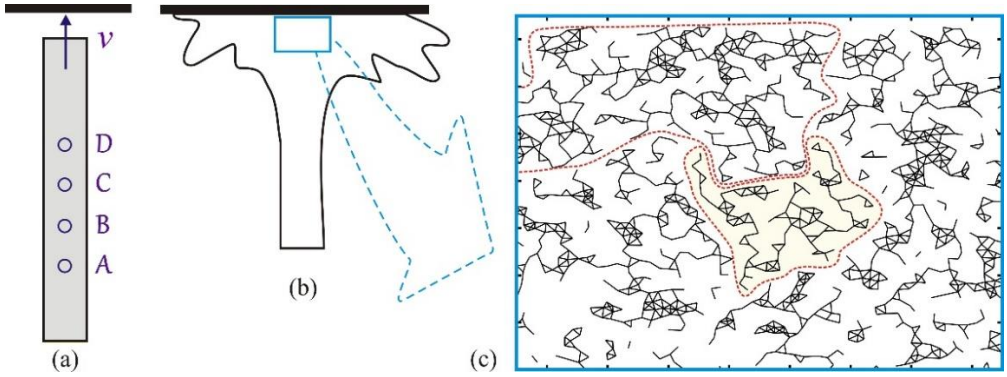

Fig. 1. Schematics of the ballistic Taylor test: the flat-nosed slender nanoprojectile impacting the rigid wall: (a) initial (the depicted four circular areas mimic the "virtual" measurement gages), and (b) severely distorted configuration. (c) Detail of the atomistic connectivity in the damage process zone attached to the contact region in the early stage of fragmentation at v = 15 km/s. Note the high connectivity in spite of the extreme damage level (reflected by the number of broken bonds). The dashed lines outline the fragments whose chainlike appearance vividly illustrate that the snapshot corresponds to a state far from equilibrium.

Fig. 2. Fragmentation snapshots corresponding to: (a) the moment of projectile arrest at v = 1 km/s, and (b) the full fragmentation at v = 3 km/s. Note how the projectile at striking velocity approaching the hypervelocity impact threshold dissolves in a cloud of fragment debris without the residual stump.

From the standpoint of Solid Mechanics, the key mechanisms of fragmentation are the nucleation, evolution, interaction, and coalescence of cracks and voids at various spatial scales (Wang et al., 2021). These "ingredients" combined account for irreversible kinetic processes inherent to numerous physical phenomena that cover a truly vast range of spatial and temporal scales. The ultrafast flat-end collision of the projectile with the rigid target is an akrological event characterized by extremely steep gradients of state variables (e.g. Mastilović 2016), well documented by shock experiments (e.g. Trunin et al. 1989). By playing the role of a "virtual microscope", MD offers a unique ability to study the dynamic fragmentation induced by strong, rapidly changing, and spatially non-uniform fields. The enormous buildup of pressure results in sequential fractures and cooperative phenomena among outcomes of these damage events that culminate eventually in energetic expulsion of fragment debris. Since the shock wave excitation is inherently ultrafast, the present MD method requires a time resolution of the order of femtosecond to observe the collective dynamics of the nanosystem. Moreover, the necessity to reach the stationary fragment distribution renders simulations extremely computationally expensive.

Traditionally, the fragmentation process was considered statistically well posed if any point of the fragmentation domain was equally likely to fracture. Such problems were easier to attack by conventional methods of mathematical physics, prior to and in the infancy stage of computational mechanics. An emblematic example of such tacit assumption of statistical

homogeneity is the uniform expansion of a ring analyzed in the Mott's seminal paper (1947). Needless to say, in engineering applications, the homogeneous fragmentation is rarely achieved due to complexity of the device geometry and the dynamic loading itself that cause the fracture intensity and, consequently, the average fragment size to be a function of position. An attempt was made by Mastilovic (2016) to explore a transition from statistically heterogeneous to homogeneous impact fragmentation by verifying to what extent the classic results of the MD simulations of the homogeneous adiabatic expansion of Holian and Grady (1988) remained valid for a highly unidirectional fragmentation process caused by application of a nonuniform transient strain-rate field. The basic premise was that given sufficient energy any point of the fragmentation domain was equally likely to fracture even in the latter case. It was demonstrated that the multilinear exponential fragment mass distribution is useful equally well for the highly nonuniform fragmentation as for the uniform one. Grady and Winfree (2001) demonstrated that the cumulative exponential fragment mass distribution follows from statistical mechanics principles.

The extensive theoretical, experimental and computational investigations of the fundamental principles of dynamic fragmentation resulted in a vast literature, which is systematically reviewed in Grady (2005), Elek and Jaramaz (2009), Ramesh et al. (2015). Computational techniques utilized in the last three decades in the dynamic fragmentation investigations start with the old war horse of the computational mechanics – the finite element method, sweep over the extensive area of the computational mechanics of discontinua, and include the meshfree methods; a rather extensive set of selected references concerning these techniques is available in references (Mastilović 2015, 2019a; Myagkov 2021).

The projectile-wall impact configuration used in this investigation (illustrated in Figs. 1-3) is the classic Taylor model arrangement allowing for the fully unconstrained lateral motion of matter upon right-angle collision with a flat target. This configuration is, due to the small dimensions, expected to be strongly influenced by surface effects.

The multilinear exponential fragment mass distribution was used extensively in previous studies in conjunction with a logarithmic binning (Mastilović 2015), as an expedient approach to explore the MD simulation results obtained by the present computational setup. Namely, it has been established that this approach was a convenient first approximation for modeling of the key features of the fragment mass distribution for the relatively small specimen size such as the one used herein. The aim of the current article is focused on an intriguing observation of a certain receptiveness and regularity emerging, fortuitously or not, from the fragment mass distributions (Mastilović 2015). Specifically, as an example, the evolution of the dominant part of the fragment distribution in the course of 30-km/s impact appeared to be characterized by a set of well-defined discrete distribution coefficients (μ_2) (refer to Fig. 3b for the clarification of notation). Moreover, the seemingly well-defined discrete μ_2 levels apparently reduce by factor of two in the course of the fragment distribution evolution. (For more details consult Mastilovic (2015), Table 2 and Fig. 4.) Interestingly, the same discreteness re-emerges from the *stationary* fragment mass distributions across the whole hypervelocity impact velocity range ($3 \text{ km/s} \leq v \leq 30 \text{ km/s}$) explore in the present investigation.

The outline of the paper organization is as follows: in Section 2 the basic method of the traditional MD is succinctly presented with emphasis on the fundamental relations, used to evaluate the parameters of state within the given simulation framework. This is followed by the brief introduction of the computational setup well known from the previous work. Section 3 outlines the main observations pertinent to the limited investigation objective to explore the apparent discreteness of the fragment mass distribution. It is shown, in the same section, that the repetitiveness and discreteness observed in the fragment mass distribution cannot be explained

by similar observations of the time histories of the selected state parameters. Finally, the conclusions are presented in the closing section.

2. Fundamental relations

The present investigation is based on the traditional MD in which the dynamic state of the atomic system is defined by laws of classical mechanics with atomic motions being uniquely determined by an empirical potential (Mastilović 2019a). A monatomic system is comprised of atoms of equal masses (m_0) that form an ideal defect-free lattice of hexagonal unit cell free of quenched disorder (Fig. 3a). The problem is deterministic since the individual atomic positions ($\boldsymbol{r}_i$; $i = 1, N_{at}$) and momenta ($\boldsymbol{p}_i = m_0 \boldsymbol{r}_i$) completely describe the interatomic interactions (e.g. the interatomic force $\boldsymbol{f}_{ij}$).[1] The Lennard-Jones model parameters, selected to match as close as possible the physical properties of tungsten ($_{74}$W), are: the atomic mass 3.1×10^{-25} kg (183.85 u), the atomic radius 1.4 Å, and the depth of the potential well (the strength of the attraction) 7.5×10^{20}J. The monocrystalline nanoprojectile is set to zero temperature prior to the impact which implies that "the jigglings and wigglings of atoms" (Feynman 1963) are nonexistent initially (Fig. 3a). The rough rigid target is represented by a set of immovable atoms.

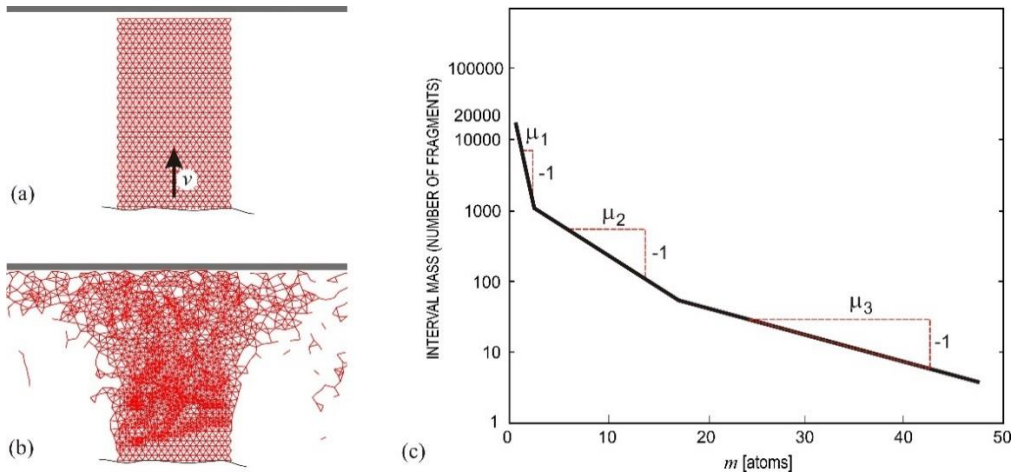

Fig. 3. (a) A portion of an ideal defect-free lattice of hexagonal unit cell that mimics a monatomic nanoprojectile prior to collision with the rigid wall. The nodal points represent atoms while the solid lines among them represent interatomic forces. (Note that the size of the projectile detail is significantly reduced in the lateral direction in this plot to improve visibility for illustrative purposes.) (b) A detail of a highly distorted nanoprojectile configuration in the early stages of the 15-km/s impact. (Note the nicely visualized shock wave front that separates the highly compressed, distorted and damaged part of the projectile from the undisturbed one.) (c) Schematic representation of the trimodal exponential fragment mass distribution used throughout this study.

The dynamics of the present atomic system approximation is completely defined by interatomic forces. These are, in turn, defined by the interatomic potential. In MD simulations from the 1950s to the 1980s, a couple of pair potentials were used almost exclusively due to the

[1] The alphabetic indices, hereinafter, refer to a particular atom, while the Greek letter subscripts are reserved for tensorial notation.

modest computer capabilities. These simplified potentials define the interatomic forces exclusively in terms of interatomic distance. Therefore, they cannot provide a quantitative description of system dynamics in more complex systems (Ercolessi1997) such as, for example, strongly covalent systems, most ceramics characterized by fully populated orbitals, metals characterized by delocalized "sea of electrons", or semiconductors. Significant progress was made during the 1980s with the development of many-body potentials for metals based on the concept of atomic density (e.g. Mishin et al. 1999). The crucial experimental observation that needed to be captured was that interatomic bonds become weaker when nested in a "dense" local atomic environment. Accordingly, a force acting on an atom depends not only on the distance separating its nucleus from nuclei of its neighbors ($\boldsymbol{r}_{ij}$), but also on the local atomic density ($\bar{\rho}_i$). Among these, so called many-body, potentials, the most popular is the embedded atom method

$$\Phi\left(\boldsymbol{r}_{ij},\rho_i\right)=\frac{1}{2}\sum_i\sum_{j\neq i}\varphi\left(\boldsymbol{r}_{ij}\right)+\Psi=\sum_i\left[\frac{1}{2}\sum_{j\neq i}\varphi\left(\boldsymbol{r}_{ij}\right)+\psi\left(\bar{\rho}_i\right)\right],\quad \bar{\rho}_i=\sum_{j\neq i}\rho\left(r_{ij}\right) \tag{1}$$

developed to approximate the interaction between ions in metals. The various forms of (1) differ from each other only in the forms of functions: φ (pairwise term depending entirely on the mutual distance of the interacting particles), ψ (density-dependent contribution - the embedding energy necessary to insert the *i*-th atom into the background of the electron density), and ρ_{ij} (atomic density function) (Mishin et al. 1999).

1.1 Evaluation of the instantaneous kinetic temperature

The estimate of temperature evolution during extreme dynamic events, which is of crucial analytical importance, gives rise to some fundamental questions related to basic thermostatic concepts such as entropy and absolute temperature of a system that is far from equilibrium. At some point, these issues were discussed in details. The excerpts of these discussions and some of the key references that pertain to it are available in (Mastilović 2019a). Herein it is deemed sufficient just to echo the Callen's (1961) assertion that the alternative nonequilibrium entropy definitions are dependent upon uncertain premises. Therefore, a consensus was established finally within the MD community that the most prudent approach was to use the Gibbs' temperature definition, familiar from the kinetic theory

$$T=\frac{1}{k_B}\left\langle \boldsymbol{p_i}\frac{\partial \mathcal{H}}{\partial \boldsymbol{p_i}}\right\rangle=\frac{1}{D\,N_i\,k_B}\left\langle\sum_{\boldsymbol{j=1}}^{\boldsymbol{N_i}}\frac{\boldsymbol{p_i^2}}{2m_0}\right\rangle\Rightarrow \mathsf{T}_i=\frac{m_0}{D\,N_i\,k_B}\sum_{j=1}^{N_i}\left(v_{xj}^2+v_{yj}^2\left[+v_{zj}^2\right]\right),\ \left(i=1,...,N_{at}\right) \tag{2}$$

where $\mathcal{H}$ is Hamiltonian, D is the dimensionality of the problem (e.g. 2D ↔ D ≡ 2 and the square brackets omitted), k_B is the Boltzmann's constant, N_i is the number of atoms of mass m_0 (belonging to the whole sample or to one of the averaging area (Fig. 1a)), while v_x, v_y and v_z are the vibrational velocity components obtained by subtracting the velocity of correlative motion from the total particle velocity. The 2D-MD counterpart of Eq. $(2)_2$ is discussed in detail by Mastilovic (2016), thus, only a brief summary is presented herein. The total velocity follows directly from the solution of Newton's equations of motion while the velocity of correlative motion is obtained as the spatial average of total velocities of all atoms belonging to one of the averaging area illustrated schematically in Fig. 1a. The temperature definition (2) has the firm statistical-mechanics foundations since it follows from the canonical ensemble maximum-probability distribution (Hoover 1985). It has been verified by the statistical hypothesis testing that the vibrational velocities obtained from these MD simulations represent a random sample corresponding to Maxwell-Boltzmann distribution (Mastilović 2017). Hoover and coworkers (1993) argued that the standard temperature definition (2) could be applied to any stable configuration regardless weather in equilibrium or not. Indeed, "in nonequilibrium situations, the

instantaneous kinetic temperature is the only meaningful definition" (Callen 1961). The instantaneous kinetic temperature (2) is averaged in both time (in accordance with the ergodic hypothesis) and space. The averaging area is commonly assumed to be the same circular region used for calculation of the velocity of correlative motion (Fig. 1a).

1.2 Evaluation of the stress, strain and effective stiffness

The expression for the components of the mechanical stress tensor at the scale of small sets of atoms is obtained as the linear (second) term in the Taylor series expansion of the potential energy of the system (e.g. Mastilovic 2019a). Notably, the stress tensor, thus obtained, is a general thermodynamic relation independent of the applicability of Hooke's law. For the embedded atom method (1), the stress tensor components are

$$\sigma_{\alpha\beta} = \frac{1}{2\Omega N}\sum_{\substack{i,j \\ j\neq i}} \boldsymbol{r}_{ij} \otimes \boldsymbol{f}_{ij} + \frac{d\,\Psi}{d\,\Omega}\delta_{\alpha\beta} = -\frac{1}{2\Omega N}\sum_{\substack{i,j \\ j\neq i}} f_{ij}\frac{\left(r_{ij}\right)_\alpha \left(r_{ij}\right)_\beta}{r_{ij}} + \frac{d\,\Psi}{d\,\Omega}\delta_{\alpha\beta} \tag{3}$$

where Ω is the average volume per atom, symbol $\otimes$ denotes the tensor product of two vectors, while $(r_{ij})_\alpha$ and $(r_{ij})_\beta$ are corresponding (α and β) projections of the distance vectors $\boldsymbol{r}_{ij}$ (Vitek, 1996; Egami, 2011). Since the stress definition (3) is inherently related to the static equilibrium state, it is rigorously applicable only to (quasi-)static deformation where the resultant force acting on each atom are ("close enough" to) zero. On the other hand, dynamic deformation implies wave propagation (Fig. 3b) and, in order for stress expression (3) to be applicable, it must be tacitly assumed that the nonequilibrium process can be represented by a successive series of equilibrium processes. (The dilemma already encountered in the temperature discussions that yielded Eq. (2).) This concept is routinely used, out of necessity, in thermodynamics of nonequilibrium processes. It should be noted that the mechanical stress, defined by interatomic forces and atomic positions (3), becomes physically ill-defined as a measure for the mean mechanical force between material points when the averaging area, in the course of fragmentation, becomes incompletely occupied by atoms.

The strain is calculated by comparing the lattice current configuration with the reference configuration. Since the information about the atomic position is readily available in both configurations, the calculation of the strain is straightforward. For example, the components of the left Cauchy-Green strain tensor of atom *i* in 2D systems are commonly defined by

$$\varepsilon = \sum_{j=1}^{6}\frac{\boldsymbol{r}_{ij}\otimes\boldsymbol{r}_{ij}}{3\,r_0^2}, \quad \varepsilon_{\alpha\beta} = \sum_{j=1}^{6}\frac{\left(r_{ij}\right)_\alpha\left(r_{ij}\right)_\beta}{3\,r_0^2} \tag{4}$$

The other strain measures can be obtained from Eq. (4). It should be noted that, unlike the stress counterpart (3), the virial strain (4) is valid *instantaneously* in time and space. Note also that Eq. (4) represents meaningful strain definition with respect to the reference state only as long as neighbors do not enter or leave the "list of neighbors" for any particular atom (the list is presented, for example, by Mastilovic 2019a), which is a rather severe limitation in the present circumstances that requires carefull scrutiny. In the case of extremely large deformations followed by large mass transport, it is more advisable to use a natural, Seth-Hill definition of relative deformation (Mastilovic 2019a).

Finally, the third term in the Taylor series expansion of the potential energy (1) defines the elastic stiffness tensor

$$C_{\alpha\beta\gamma\delta} = \frac{1}{2\Omega N}\sum_{\substack{i,j \\ j\neq i}}\left(\frac{d^2\varphi}{dr_{ij}^2} - \frac{1}{r_{ij}}\frac{d\varphi}{dr_{ij}}\right)\frac{\left(r_{ij}\right)_\alpha\left(r_{ij}\right)_\beta\left(r_{ij}\right)_\gamma\left(r_{ij}\right)_\delta}{r_{ij}^2}$$
$$-\frac{1}{2}\frac{d\Psi}{d\Omega}\left\{\left(\delta_{\alpha\gamma}\delta_{\beta\delta}+\delta_{\beta\gamma}\delta_{\alpha\delta}\right)\left(2-\delta_{\alpha\beta}\right)-\frac{1}{2}\delta_{\alpha\beta}\delta_{\gamma\delta}\left(4-\delta_{\alpha\gamma}-\delta_{\beta\gamma}-\delta_{\alpha\delta}-\delta_{\beta\delta}\right)\right\} \quad (5)$$
$$+\Omega\frac{d^2\Psi}{d\Omega^2}\delta_{\alpha\beta}\delta_{\gamma\delta}$$

Obviously, for the pair potentials $\Psi = 0$, as in the case of results presented herein, and only the first terms of Eqs. (3) and (5) remain. When the embedded-atom (1) or related methods are used to model interatomic interactions, it is necessary to use the complete Equations (3) and (5) that take into account the density (the average volume per atom) dependence of the potential.

1.3 The closing remarks on the MD fragmentation model

The conversion of simulation data generated at the nanoscale level (***r***, ***v***, ***a***) to macroscopic observables ($\boldsymbol{\sigma}$, $\boldsymbol{\varepsilon}$, ***C***, *T*), summarized above, is firmly established nowadays. As for the fragment definition for the current model, an interatomic bond ruptures when the distance between the corresponding atoms exceeds a predetermined critical value $\underline{R}$. Consequently, a fragment is defined as a self-bound cluster of atoms with interatomic distance less than the cut-off distance ($r \leq \underline{R} \approx 1.7\, r_0$). The critical distance is arbitrarily selected to be between the first and second nearest neighbors in the reference triangular configuration of the perfect crystal (Mastilovic 2015, 2016).

As elaborated in detail in preceding articles (Mastilovic 2015, 2017), this fragmentation model is generic in the sense that it aims to capture the underlying nanoscale-fragmentation physics. Its simplicity rests primarily on the 2D geometry, the elementary potential, and nanoscale projectile dimensions. Although the dimensionality of the system is known to influence shock physics and the universality classes of fragmentation phenomena, the 2D choice is necessitated by computational economy and justified by a qualitative nature of the study. Furthermore, it has been demonstrated not so long ago that for a similar MD simulation technique "the fragmentation features of the system are not sensitive to the number of particles" and that fragmenting systems seemingly share the same generic behaviors regardless of the details of their interaction potentials (Sator et al. 2008). Although the size of the current model exceeds those used by Sator and coauthors (2010), similarly utilizing 2D-MD to investigate generic behavior in the impact fragmentation, it goes without saying that the present study would benefit from the model size increase resulting in the fragment sample increase and, consequently, the more robust postprocessing. Finally, it is indicative for the present study that its author previously demonstrated (Mastilovic 2019a) that the kinetic energy associated with shattering fragmentation is insensitive either to the initial temperature of the nanoprojectile (0 vs. 1000 K) or the choice of the interatomic potential (Lennard-Jones vs. embedded atom method).

3. Observations

With reasonable generality, it can be asserted that the kinetic energy K_0 of the impacting projectile is partitioned among the kinetic energy of the fragment debris expulsion and the various forms of the dissipation energy absorbed by the projectile

$$K_0 = K_1 + E_p + E_{th} + E_f \quad (6)$$

In Eq. (6), K_1 is the kinetic energy of the motion of fragments upon the impact, E_p is the energy of plastic dissipation, E_{th} is the energy of shock-induced heating, and E_f is the fracture energy dissipated through creation of new surfaces and ensuing fragmentation.

If the fragment mass, m, is considered a scalar variable, the random statistically non-uniform fragmentation for the striking velocities barely exceeding the threshold of complete projectile fragmentation (i.e., $v = \{3, 4, 5\}$ [km/s] for the present system) can be represented by the trimodal form of the Poisson hyper-exponential distribution:

$$N(m) = \frac{M(m)}{m} = N_{01}\exp\left(-\frac{m}{\mu_1}\right) + N_{02}\exp\left(-\frac{m}{\mu_2}\right) + N_{03}\exp\left(-\frac{m}{\mu_3}\right), \quad N_{0i} = \frac{M_{0i}}{m} \tag{7}$$

where: N is number of the n-atom fragments of mass $m = n \cdot m_0$, $M = N \cdot m = N \cdot (n \cdot m_0)$ – total mass of all n-atom fragments, and (μ_1, μ_2, μ_3) – a set of distribution coefficients representing slopes in the semilogarithmic space (Fig. 3c).

The trimodal-exponential form (7), illustrated in Fig. 3c, includes the following three distribution regions:

(i) The small tail (narrow shoulder; μ_1) of the distribution defined by the miniscule (for the present MD simulation framework, largely monatomic and biatomic) fragments the most numerous by far;

(ii) The medium-fragment distribution region (μ_2) encompassing the overwhelming number of existing *fragment classes* and the most representative part of the fragment population (away from the distribution tails), which is in the focus of the present investigation; and

(iii) The large tail (wide shoulder; μ_3) of the distribution defined by the largest fragments.

In general, for the fragmentation on the mesoscale and macroscale, the small tail of the distribution is, in the experimental (and consequently, analytical) analyses often disregarded due to both the detection limits of experimental techniques and the negligible importance. On the other hand, the large tail is, more often than not, of substantial interest. (As an example, the largest fragments provide inputs for design basis events such as the secondary impacts for the space structures.) Accordingly, a large amount of work is dedicated to the analytical description of the large tail.

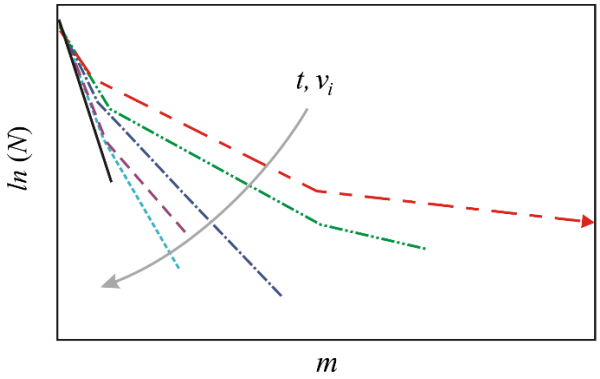

Fig. 4. Schematic representation of the effect of increase of the energy dissipated in a shock-compression process on the fragment distribution. The energy increase indicated by the arrow could be either due to the increase of the striking velocity (Fig. 3) or the duration of the fragmentation process (given sufficient energy) at the fixed striking velocity (Fig. 5). (Adopted from (Mastilović 2015)).

The impact energy delivered to the fragmenting system depends on the striking velocity and the duration of the fragmentation process. The increase of this imparted energy, designated with K_0 in Eq. (1), results in the fragment-distribution transformation captured by the trend $\mu_3 \rightarrow \mu_2 \rightarrow \mu_1$ depicting the gradual reduction of the maximum fragment mass (Mastilović 2015). According to the MD simulation results presented in Fig. 5a, for the striking velocities exceeding 5 km/s, the trimodal-exponential fragment distribution transforms into the bimodal. Consequently, the large tail of the distribution—important as it may be for the moderate hypervelocity impacts—merges with the medium-fragment region for all $v > 5$ km/s and the most representative set of fragments (all but the smallest) is captured completely by the fragment distribution region defined by μ_2.

A continuing trend toward the linear exponential distribution, $\mu_2 \rightarrow \mu_1$, is apparent from Fig. 5a for all other striking velocities $v > 5$ km/s. Finally, for the pair of ultrahigh striking velocities $v = \{20, 30\}$ [km/s], the two distribution modes are barely distinguishable on the semilogarithmic plot indicating the transformation from the bimodal-exponential to the linear-exponential distribution. This trend of the maximum fragment mass reduction with the energy increase, finally results in the asymptotic approach to the shattering transition characterized by a deterministic monatomic fragment distribution ($m_{max} \equiv 1$) (Mastilović 2019b).

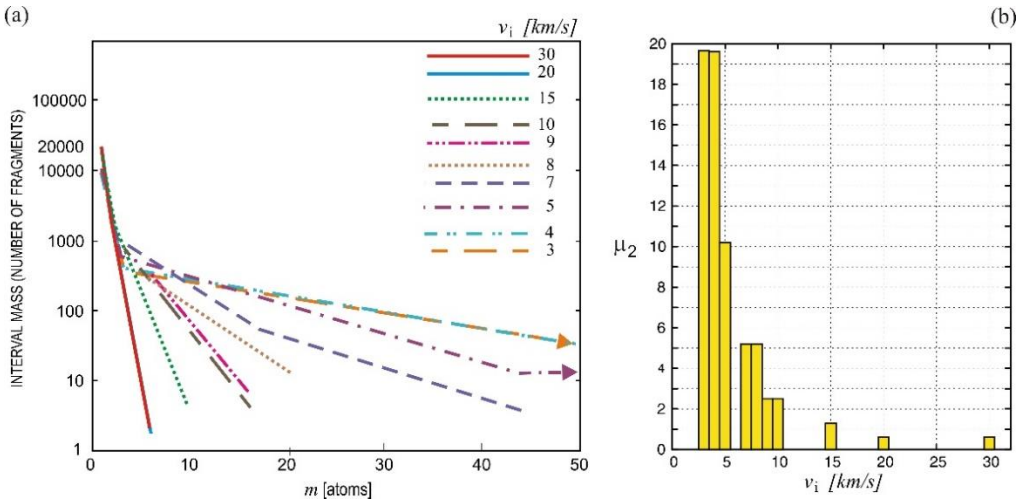

Fig. 5. (a) Semilogarithmic plot of stationary cluster statistics—the normalized bin mass vs. the fragment mass ($m=n \cdot m_0$)—emphasizing (b) the evolution of μ_2 coefficients in the hypersonic striking velocity range.

The present investigation is focused on this, arguably, the most representative, part of the fragment distribution and the corresponding distribution coefficient μ_2. Specifically, as noted in Introduction, it has been observed that:

i. the evolution of the fragment mass distribution in time (Mastilovic 2015), and

ii. the stationary fragment mass distribution for various striking velocities in the hypersonic range (Fig. 5a),

are not defined by an arbitrary spectrum of μ_2 coefficients but rather a discrete set of reoccurring values. In other words—given sufficient impact energy— μ_2 evolves in cascading manner by making “discrete leaps” between the seemingly “admissible” values. Furthermore, the

same set of μ_2 coefficients emerges in the stationary distributions for the entire hypervelocity impact range.

The observed set of values of μ_2 coefficient, illustrated in Fig. 5b, could be captured by the following expression:

$$\mu_2 = \frac{2^k}{\pi}, \quad (k = 1,\ 2, 3, 4, 5, 6) \tag{8}$$

where the lowest exponent value (k = 1) corresponds to the pair of ultrahigh striking velocities v = {20, 30} [km/s].

An attempt is made to relate the discrete and seemingly well-defined change of μ_2 coefficient (8) to some feature of the state parameters time history. The state parameters explored include the instantaneous kinetic temperature (2), the stress (3) and strain (4) components, the effective strain, the pressure ($(\sigma_{xx} + \sigma_{yy})/2$) and the stress difference ($(\sigma_{yy} - \sigma_{xx})/2$). An example of this postprocessing effort is illustrated by the results presented in Fig. 6 that are limited to temperature and pressure in two measurement areas corresponding to the middle section of the nanoprojectile (*C* and *D* according to the notation of Fig. 1a). The time histories of Fig. 6 reveal the continuous change of both temperature/pressure levels and are rated for the three striking velocities, which is according to our intuitive expectation. Consequently, the exploration of time histories of the enumerated state parameters offers no hint at the physical cause of the discrete character of μ_2 coefficient (8) of the fragment mass distribution (7).

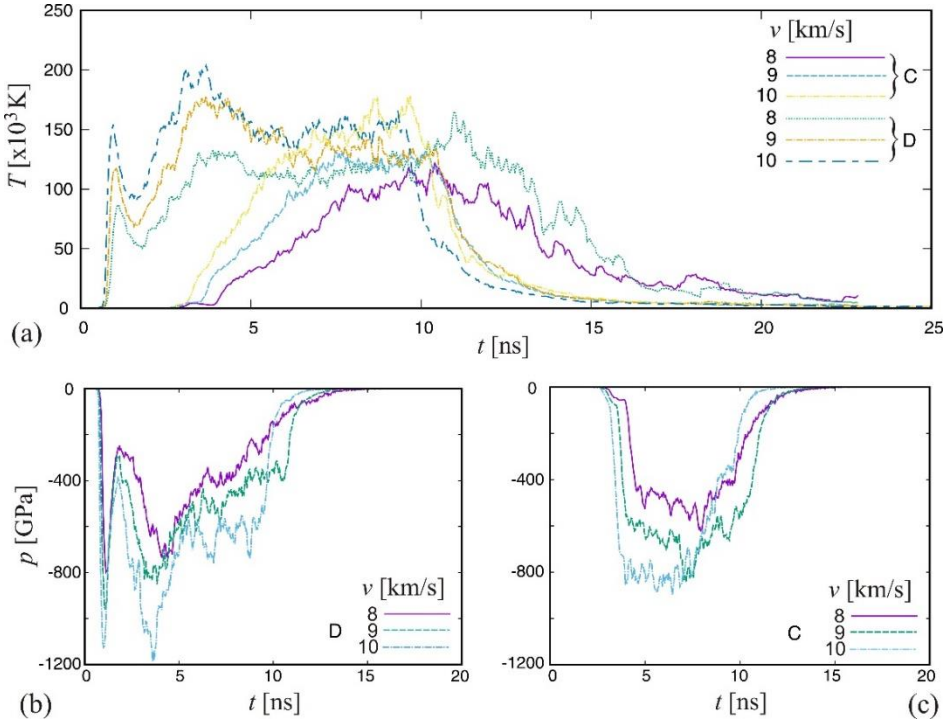

Fig. 6. Example of time histories of two selected state parameters: (a) temperature recorded at the measurement areas *C* and *D*, (b) pressure, $(\sigma_{xx} + \sigma_{yy})/2$ at *D*, and (c) pressure at *C*. The measurement area designation refers to Fig. 1a. The striking velocities v = {8, 9, 10}[km/s] correspond to μ_2 = {5.2, 2.5, 2.5}, respectively.

4. Conclusions

A simple generic 2D-MD model of the rigid-anvil impact is used in this study to address an intriguing observation of an apparent discreteness of the fragment distribution at the nanoscale, which emerged from preceding work. The striking velocities used in this investigation cover the hypervelocity range (3 km/s $\leq v \leq$ 30 km/s) corresponding to projectiles being fully fragmented upon impact. The Poisson hyper-exponential distribution with the logarithmic binning is used to capture the fragment mass distribution under the constraint of a small sample size. Specifically, the fragment population is approximated by a trimodal form of this distribution for the striking velocities $v = \{3, 4, 5\}$ [km/s], which are slightly in excess of the threshold velocity of the complete projectile fragmentation. For the remaining striking velocities ($v \geq 7$ km/s), the bimodal form of the approximation suffices. Under these circumstances, μ_2 (and μ_3, when applicable) coefficients of the Poisson distribution capture the majority of the fragment classes; that is, all but the smallest fragments captured by μ_1, which are frequently disregarded in fragmentation studies.

The gist of the present investigation is that the observed values of μ_2 coefficients suggest certain repetitiveness and discreteness. This peculiar "quantization" of μ_2 values occurs both during the time evolution of the fragment mass distribution and in the stationary state across the striking velocity field. In other words, given sufficient impact energy, μ_2 evolves in cascading manner by making "discrete leaps" between "admissible" values until it settles into the final steady state. The same set of μ_2 values emerges from the stationary distributions for the entire hypervelocity impact range. This implies that μ_2 coefficients (describing all but the smallest fragment classes in the hypervelocity impact range) are not defined by an arbitrary spectrum of values but rather a discrete set. This discrete set obtained from MD simulations {0.60, 1.3, 2.5, 5.2, 10.3, 19.6}, exhibits a simple regularity: the values could be approximated by various successive powers of 2. Consequently, an empirical expression, $2^k/\pi$, (k = 1, 2, 3, 4, 5, 6), is offered that captures the above discrete set.

An attempt is made to relate the observed repetitiveness and discreteness to some feature of the time histories of the selected state parameters in the early stages of the nanoprojectile deformation and fragmentation. This effort proved futile since no repetitiveness and discreteness in those time histories was revealed, which would hint at the observed repetitiveness and discreteness of μ_2 values. The time history features were as intuitively expected: namely, the continuous increase of the kinetic energy imparted to the fragmenting system resulted in *continuous* increase of the parameter levels and rates observed in the time histories. Therefore, since the physical explanation for this peculiar observation is lacking at present, the mere existence of the phenomenon must be brought into question. Consequently, to begin with, it would be beneficial to verify these simulation results on substantially larger systems (e.g., one order of magnitude), which would ensure more representative sample size and, consequently, more reliable results. This averment is based on a long-established rule that every statistical analysis benefits from the sample size increase. In that case, it would be possible to judge more confidently whether the femtosecond fragmentation process at the nanoscale truly exhibits this unique and interesting feature. Be it as it may, no matter how large the nanoprojectile, the "wide-shoulder" bins would nonetheless be relatively sparsely populated, especially for the higher striking velocities.

Acknowledgement: The author acknowledges support of the Ministry of Education, Science and Technological Development of the Republic of Serbia.

References

Callen HB (1961). *Thermodynamics*, John Wiley & Sons, New York, USA.

Egami T (2011). Atomic level stress. Progress in Material Science, 56, 637–653.

Elek P, Jaramaz S (2009). Fragment mass distribution of naturally fragmenting warheads. *FME Transactions*, 37, 129.

Ercolessi, F (1997). *A molecular dynamics primer*. Spring College in Computational Physics, ICTP, Trieste, Italy.

Feynman RP (1963). *The Feynman Lectures on Physics*, Addison-Wesley, Boston, USA.

Grady DE (2006). *Fragmentation of Rings Shells*, Springer, Berlin, Germany.

Grady DE, Winfree NA (2001). Impact fragmentation of high-velocity compact projectiles on thin plates: A physical and statistical characterization of fragment debris. *International Journal of Impact Engineering*, 26, 249-262.

Holian BL, Grady DE (1988). Fragmentation by Molecular Dynamics: The Microscopic "Big Bang." *Physical Review Letters*, 60(14), 1355-1358.

Hoover WG (1985). Canonical dynamics: Equilibrium phase space distributions. *Physical Review A*, 31, 1695-1697.

Hoover WG, Holian BL, Posch HA (1993). Possible experiment to check the reality of a nonequilibrium temperature. *Physical Review E*, 48, 3196-3198.

Mastilovic S (2015). Impact fragmentation of nanoscale projectiles at ultrahigh striking velocities. *Meccanica*, 50, 2353-2367.

Mastilovic S (2016). Molecular-dynamics simulations of the nanoscale Taylor test under extreme loading conditions. *Mathematics and Mechanics of Solids*, 21(3), 326-338.

Mastilovic S (2017). Damage-fragmentation transition: Size effect and scaling behavior for impact fragmentation of slender projectiles. *International Journal of Damage Mechanics*, 27(2), 201-217.

Mastilovic S (2016). Molecular-dynamics simulations of the nanoscale Taylor test under extreme loading conditions. *Mathematics and Mechanics of Solids*, 21(3), 326-338.

Mastilovic S (2019a). *Computational Mechanics of Discontinua: Fundamentals and Applications in Fragmentation*. Institute for Multidisciplinary Research, University of Belgrade (in Serbian).

Mastilovic S (2019b). Shattering impact fragmentation of slender nanoprojectiles, *Meccanica*, 54(14), 2295-2306.

Mishin Y, Farkas D, Mehl MJ, Papaconstantopoulos DA (1999). Interatomic potentials for monoatomic metals from experimental data and ab initio calculations. *Physical Review B*, 59, 3393-3407.

Mott NF (1947). Fragmentation of shell cases, *Proceedings of the Royal Society of London*, A189, 300-308.

Myagkov NN (2021). Critical behavior for impact fragmentation of spherical solid bodies sensitive to strain rate. Journal of Statistical Mechanics: Theory and Experiment 2021, 113201

Ramesh KT, Hogan JD, Kimberley J, Stickle, A (2015). A review of mechanisms and models for dynamic failure, strength, and fragmentation. *Planetary and Space Science*, 107, 10-23.

Sator N, Mechkov S, Sausset F (2008). Generic behaviours in impact fragmentation. *European Physics Letters*, 81, 44002.

Sator N, Hietala H (2010). Damage in impact fragmentation, *International Journal of Fracture*, 163, 101-108.

Trunin RF, Medvedev AB, Funtikov AI, et al. (1989) Shock compression of porous iron, copper, and tungsten, and their equation of state in the terapascal pressure range. *Soviet Physics JETP (J. Exp. Theor. Phys.)* 68, 356–361.

Vitek V (1996). Pair potentials in atomistic computer simulations. In: Interatomic potentials for atomistic simulations, *MRS Bulletin,* 21, 20-23.

Wang J, Wu B, He A (2021). Research Progress on Dynamic Damage and Failure of Metal Materials under Shock Loading with Molecular Dynamics Simulation. Chinese Journal of High Pressure Physics 35(4), 040101.